Archive of Applied Mechanics (2025) 95:66
https://doi.org/10.1007/s00419-025-02770-2

ORIGINAL

Burcu Küçükoğlu Doğan · Abdurrahim Dal · Tuncay Karaçay

Modeling hybrid polymer ball bearing with elastoplastic contact model and its nonlinear dynamic response

Received: 20 May 2024 / Accepted: 27 January 2025 / Published online: 13 February 2025

Abstract The dynamic behavior of a polymer ball bearing system is mostly dependent on the contact characteristics among the ball and the races of the bearing. Although the well-known Hertz contact theory is widely used to model contacts in conventional bearings, it cannot be directly applied to polymer bearings due to the viscoelastic characteristics of the polymer structures. In this study, contacts in the polymer hybrid ball bearing are modeled using elastoplastic characteristics. The contact between inner/outer raceways and the ball is solved in elastic, elastoplastic, and plastic characteristics regions depending on the polymer structure and the loads. Then, two-degree of freedom rigid rotor-bearing system is simulated under different rotational speeds as well as different rotor weights. In order to investigate the nonlinear nature of the dynamic response, results are analyzed with different methods such as waterfalls, bifurcation diagrams, phase diagrams and Poincaré sections. The characteristic changes in the contact form elastic to elastoplastic regions are observed as a new peak in the time history that may lead to chaotic motion. A similar response is also seen when a single ball-race contact is in the elastoplastic region. The results are helpful to understand the cause and result of contact in a viscoelastic contact condition.

Keywords Polymer hybrid ball bearing · Elastoplastic contact · Nonlinear dynamic

List of symbols

A	Contact area (m^2)
A'	Truncated area (m^2)
a'	Radius of the truncated contact area (m)
d_b	Diameter of the ball (m)
d_m	Pitch diameter (m)
d_i	Inner raceway diameter (m)
d_o	Outer raceway diameter (m)
D_i	Inner race diameter (m)
D_o	Outer race diameter (m)

B. K. Doğan (✉)
Mechanical Engineering Department, Muş Alparslan University, Muş, Turkey
e-mail: b.kucukoglu@alparslan.edu.tr

A. Dal
Mechanical Engineering Department, Adana Alparslan Türkeş Science and Technology University, Adana, Turkey
e-mail: adal@atu.edu.tr

T. Karaçay
Mechanical Engineering Department, Gazi University, Ankara, Turkey
e-mail: karacay@gazi.edu.tr

E_1 Elastic modulus of balls (Gpa)
E_2 Elastic modulus of raceways (Gpa)
E' Effective elastic modulus values (Gpa)
$\mathrm{F_e}$ Elastic contact force (N)
F_{ep} Elastic–plastic small deformation contact force (N)
F_{i} I. force on ball (N)
g Gravitational acceleration (m/s^2)
M Mass of shaft (kg)
n Total number of balls
N Rotational speed (rpm)
P_x The unbalanced force along the x-axis direction (N)
P_y The unbalanced force along the y-axis direction (N)
Q Nondimensional variable of model
R The radius of the sphere (m)
r_{i} Groove Radius of inner race (m)
r_{o} Groove Radius of outer race (m)
S_{y} The initial deformed material's yield stress value (MPa)
$\omega_{\mathrm{b}p}$ Ball transition frequency (Hz)
ω_{c} Cage's angular speed (rad/sec)
ω_{i} Inner race angular speed (rad/sec)
ω_{o} Outer race angular speed (rad/sec)
ν_1 Poisson ratio of balls
ν_2 Poisson ratio of raceways
e_{u} Unbalance eccentricity (m)
w Bearing width (m)
δ Deflection between the sphere and the flat surface (m)
Δt Time step (sec)
$\overline{x}_0$ Initial condition (m)
γ The angle between two adjacent balls (rad)
$\propto$ Contact angle (degree)

1 Introduction

The use of polymer ball bearings is continuously increasing in the food and pharmaceutical factory processes due to the corrosion and contamination problems of traditional steel ball bearings. No need for lubrication is also an important advantage of these bearings. However, load and speed ratings are constraining properties of the hybrid polymer bearings that needs further development and analysis.

The operating conditions of bearings affect their dynamic characteristics. The bearings are operated in the elastic region to increase their lifetime. However, in some cases, it may exceed the elastic region. Therefore, the shaft-bearing system and contact mechanics should be considered when determining the dynamic properties of bearings. While investigating the dynamic characteristics of the shaft-bearing system, Hertz's contact theory has been preferred for conventional bearings. But an elastoplastic contact model is used because of the viscoelastic structure of polymer bearings instead of Hertz contact theory. The elastoplastic contact is examined in three regions: elastic, elastoplastic, and fully plastic. The Hertz contact model is still valid in the elastic region, however, the behavior of the contact must be investigated as fully plastic when the deformations becomes permanent. The elastoplastic region is the transition regime between fully elastic and fully plastic conditions. And, the limitations of elastoplastic contact mechanics are determined using various models and methods. Ghaednia et al. have a good review of studies on this subject [1].

Most published studies in elastic–plastic contact simplify analysis by focusing on contact point between a flat surface and a sphere [2–11]. The modeling and solving of the contact problem generally use finite element methods. The analysis of the indentation problem using the FEM was first introduced by Hardy et al. [12]. They carried out a qualitative analysis of the elastic–plastic indentation, but provided no formulas for prediction. Sinclair et al. [13] and Sinclair et al. [14] investigated indentation through the use of the finite element method, and by utilizing an improved meshing strategy, some phenomenological formulations were found. They contrasted their numerical predictions with experiments [15] and other extant theories,

including slip-line theories by Ishlinskii [16] and Richmond [17]. Komvopoulos and Ye [18, 19] defined a nondimensional variable, Q, by fitting phenomenological equations to finite element data for closed-form models. Komvopolous, and Ye's model was revised the model introduced by Kogut and Komvopolous [20], who took into account both the loading and unloading stages. Analytical model verification study in terms of contact radius in an indentation contact using experimentation and numerical methods was also carried out by Bartier et al. [21]. A semi-analytical model was recently established by Brake [22] by splitting the contact problem into three parts. Kharaz et al. [23, 24] validated this model. Brake connected the elastic and fully plastic phases using a similar technique but different transition functions in a more recent work [25]. Yau et al. [26] derived elastic and elastoplastic contact models to investigate ball bearing contact behavior, taking into account the interaction between the ball and the inner race.

The rotor system's dynamic behaviors are greatly impacted by the rolling bearing, which is frequently utilized in rotor systems. Three major factors contribute to nonlinearity in rolling bearings: defects, the gap between inner/outer races, and nonlinear restoring forces on curved surfaces in contact. The nonlinear restoring force models were developed and applied both numerically and experimentally [27–35]. Nonlinear behaviors of the rotor-bearing coupling system have been studied by numerous studies [36–40]. The finite element method is used by Lu et al. [41] to perform bifurcation analysis and dynamic modeling for a rolling bearing-rotor system. The authors also analyze the effects of the clearance and eccentricity on the vibration behavior using a lumped parameter model in another study. The bifurcation trajectory was used to analyze the results [42]. Li et al. developed a nonlinear dynamic model based on the structure of the damaged bearing. The impact of rotational speed and radial load on the nonlinear responsiveness to vibration are examined. Next, the various vibration behavior are examined when the bearing's raceways sustain damage. Lastly, a study is done on how the nonlinear characteristics are affected by the extent of shaft current damage. The findings show that when the radial load changes, the bearing system exhibits bifurcation, leaps, and chaos [43]. Ambrożkiewicz et al. derived a dimensionless mathematical model in 2-DOF for ball bearings. This model aids in scaling the issue and reveals the connections between dimensionless terms and how they affect response of the system's using the Hertzian contact theory. The resultant mathematical model takes into account nonlinear parameters such as radial internal clearance, stiffness, and dumping. A wealth of information on the system's dynamics may be found using transforms, phase plots, orbit plots, and recurrences. These tools also made it easier to identify the point at which the periodic and chaotic responses change [44]. Chang et al. analyzed the thermal coupling and nonlinear dynamic properties of bearing-rotor systems with the modified incremental harmonic balance (IHB) approach following the thermal balance [45].

The nonlinear dynamics of the shaft supported by the standard steel ball bearing has been extensively researched in the literature; however, the dynamic behavior of the hybrid polymer ball bearing-rotor system has not been thoroughly studied. Moreover, the dynamic of the system examined for elastic contact region, and the Hertz contact model is sufficient for conventional bearings. However, it is important that the viscoelastic characteristics of the polymer structure are included in the contact model for the polymer ball bearing. Thus, the purpose of the study that is being given is to look into how elastoplastic contact affects the rotor's nonlinear response when it is supported by a hybrid polymer ball bearing. To evaluate the dynamics of the system, firstly, we modeled the contact between the ball and raceways considering the elastoplastic characteristics of the structure, and we formulated the contact forces based on the contact characteristic. Then, we derived the equations of motion of the system for a 2-DOF rigid rotor-bearing system and developed an algorithm based on the Runge–Kutta method. Finally, a serial simulation was run with various shaft speeds and weights, and the system's bifurcation features were examined to study the effects of the elastoplastic contact on the system's dynamic behavior. And the nonlinear behavior of the steady-state responses was discussed on the waterfall graphs, orbit and spectrum plots, phase portraits, and Poincare section.

2 Mathematical models

Due to the viscoelastic structure of the polymer material that makes up the inner and outer races of the bearing, the ball-race contact should be analyzed using elastoplastic contact. The kinematics of the polymer bearing, the shaft-bearing system's equations utilized to generate the simulations, and the model used for elastoplastic contact in this study are all detailed in the following sections.

2.1 Elastic–plastic contact model

The contact model between the ball and raceways is based on a mathematical formulation derived by Komvopoulos and Ye, considering elastoplastic characteristics. According to this formulation, Komvopoulos and Ye [18] were identified the contact in four phases: the plastic, elastic–plastic big deformation, elastic–plastic medium deformation, and elastic phases. And using finite element analysis and phenomenological equation fitting, they created closed-form models. In these models, the nondimensional variable Q could be calculated from Eq. 1, and the contact characteristics could be determined from range of the Q value.

$$Q = \left(\frac{E'}{S_y}\right)\left(\frac{\delta}{a'}\right) \tag{1}$$

where S_y is the initial deformed material's yield stress value. δ denotes the deflection between the sphere and the flat surface, In Eq. 1, a' is the radius of the truncated contact area that ignores the flat's pile-up and sink-in deformations, and it could be computed from Eq. 2. R denotes the radius of the sphere.

$$a' = \sqrt{R^2 - (R - \delta)^2} \tag{2}$$

E' given in Eq. 1 refers to the effective elastic modulus values of the contacting materials and can be calculated as shown in Eq. 3.

$$\frac{1}{E'} = \frac{1 - v_1^2}{E_1} + \frac{1 - v_2^2}{E_2} \tag{3}$$

According to Komvopoulos and Ye model, when the Q is in a range of 0 and 1.78, the contact is in elastic phase. And, the contact force could be computed from Eq. 4.

$$\frac{F_e}{A} = \left(\frac{4\sqrt{2}}{3\pi}\right) Q(S_y) \tag{4}$$

In Eq. 4, F_e indicates the corresponding elastic contact force. In Eq. 4, A is the real area, and A' is truncated area, and they could be given in Eqs. 5 and 6, respectively.

$$A = \frac{A'}{2} \tag{5}$$

$$A' = \pi a'^2 \tag{6}$$

When the Q value is in a range of 1.78 and 21, the contact characteristic is elastic–plastic small deformation, and F_{ep} could be computed from Eq. 7.

$$F_{ep} = A(0.7\mathrm{In}(Q) + 0.66)S_y \tag{7}$$

where A could be calculated as following.

$$A = \frac{A'}{0.05(\mathrm{In}Q)^2 - 0.57(\mathrm{In}Q) + 2.41} \tag{8}$$

For the elastic–plastic medium deformation, when the Q value is in a range of 21–400, the contact force could be given as following, where A is calculated from Eq. 8.

$$F_{ep} = A(2.9)S_y \tag{9}$$

Q > 400 elastic–plastic large deformation, and A could be calculated as following.

$$A = \frac{A'}{0.71} \tag{10}$$

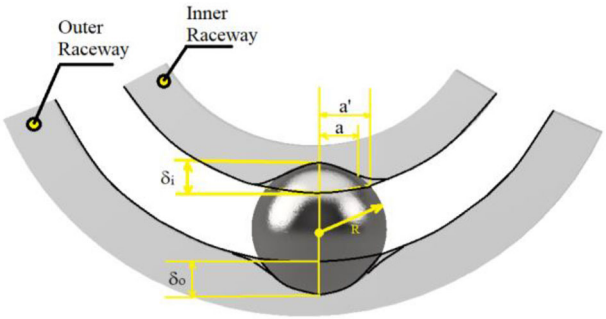

Fig. 1 Total deflection

2.2 Kinematics of the ball bearing

In bearings, force is transmitted by the deformation of the balls. The pressure force causes the balls to deform into a restricted area when they are in a specific number and position as the shaft rotates. The outer and inner races of the bearing are loaded when the deformed balls make contact with the raceway. Determining how deformation occurs in each ball is necessary to calculate the maximum load bearings can support. The quantity of deflection on each ball is expressed as the total of the deflection that occurs when the balls come into contact with the inner race (δ_i) and the deflection that occurs when the balls come into contact with the outer race (δ_o). The mathematical formula for the total deflection on the bearing is presented in Eq. 11.

$$\delta = \delta_i + \delta_o \tag{11}$$

Figure 1 illustrates how the ball deforms as a result of inner and outer race-ball contact as well as the total of the deformations.

The overall amount of load on the balls and the bearing's stiffness define the forces operating on the bearings. The total force is determined by the load that each ball carries. The more the ball is deflected, the more force is applied to the bearing.

Bearing vibrates even in perfect condition. The ball transition frequency describes this circumstance. The ball transition frequency is the product of the cage's angular velocity and ball count. Equation 12 provides a mathematical depiction of the ball transition frequency. Here, ω_c denotes the cage's angular speed and mathematical formulation is given in Eq. 13, whereas n denotes the number of balls in the bearing.

$$\omega_{bp} = n\omega_c \tag{12}$$

Only the inner race's angular velocity was taken into account for measuring the cage speed in this study since the outer race was thought to be immovable and the inner race to be moveable.

$$\omega_c = \frac{1}{2}(\omega_i(1-\gamma) + \omega_o(1+\gamma)) \tag{13}$$

Seen in Eq. 13 γ denotes the angle between two adjacent balls and it could be calculating using Eq. 14.

$$\gamma = \frac{d_b}{d_m}\cos\alpha \tag{14}$$

Given in Eq. 14 γ taken as zero since the modeled bearing is a deep groove ball bearing in this study.

2.3 Equation of motion

Equations of motion have been generated by applying certain model-based assumptions. The following is a list of assumptions in the solution:

1. Two degrees of freedom are considered for the shaft in the radial directions of x and y.
2. It is assumed that the inner race has evenly distributed balls, while the outside race remains stationary.
3. Balls are thought to have no mass,

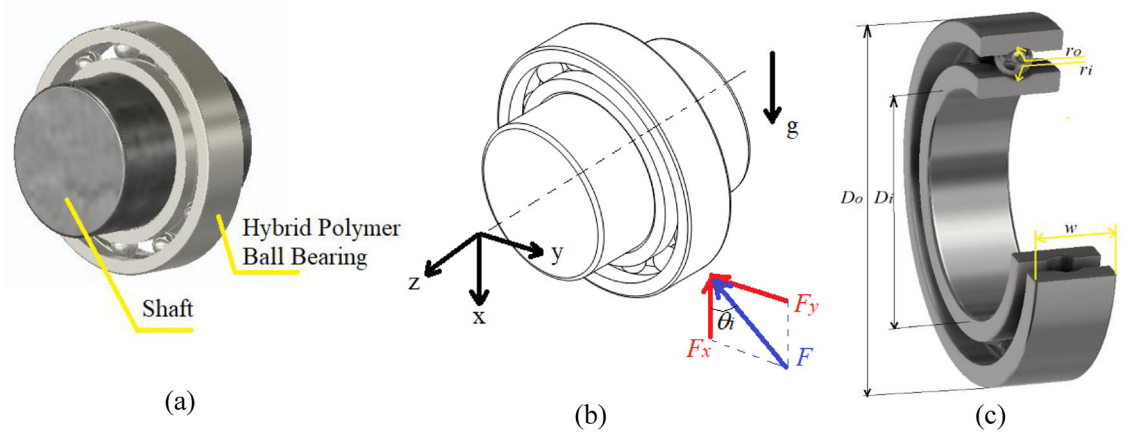

Fig. 2 Shaft-bearing system schematic views, **a** 3D view of the bearing-rotor system, **b** coordinate axis and the contact force, **c** detail of the hybrid polymer ball bearing

4. The races are stiff, and only local deformations occur,
5. One assumes that the shaft is stiff.

According to these assumptions, Eqs. 15 and 16 specify the equations of motion modeled in 2-degree of freedom, and Fig. 2 shows the shaft-bearing system schematic view.

$$M\ddot{x} + \sum_{i=1}^{n} F_i \cos(\theta_i) + P_x - \mathrm{Mg} = 0 \tag{15}$$

$$M\ddot{y} + \sum_{i=1}^{n} F_i \sin(\theta_i) + P_y = 0 \tag{16}$$

where P_x and P_y are unbalanced forces and they could be calculated from Eqs. 17 and 18. M denotes the mass of the shaft, and n denotes the number of ball.

$$P_x = -Me_u\omega^2 cos\omega t \tag{17}$$

$$P_y = -Me_u\omega^2 sin\omega t \tag{18}$$

In this study, the equations of motion are solved with the Runge–Kutta method, and the system's dynamic motion is calculated in an instant. Then, the deformations of the raceways are calculated with the kinematic relationship of the ball bearing-rotor system and displacement data from the solution of the Eqs. 15 and 16. To calculate the deformations, firstly the nondimensional variable Q is calculated from Eq. 1 for the material properties, displacement, and the radius of the truncated contact area, a' given in Eq. 2. After determining the nondimensional Q value, the contact force is computed from Eqs. 4, 7, and 9 for the range of the Q value identified for contact characteristics. Finally, this calculation procedure is applied for each ball, and the total contact force along x- and y-directions is determined with respect to the ball position given as Eqs. 15 and 16.

3 Results and discussion

The effects of the plastic and elastoplastic contact between the inner raceway-ball-outer raceway in the hybrid polymer ball bearing on the nonlinear dynamic behavior of the system responses are analyzed. The equations of the motions were numerically solved with the developed algorithm, and a serial simulation was run to investigate the behavior of the response under different contact characteristics. The operational conditions and specifications of the ball bearing-rotor system were listed in Table 1, and the bifurcation parameters were chosen as the rotational speed and the rotor mass. The steady-state portions of the simulation results were regarded to avoid the transient information in the responses, and nonlinear dynamic analysis was studied in time and frequency domains. Firstly, the response of the system was investigated with waterfall diagrams and bifurcation analysis to estimate the critical speeds, as well as the nonlinear behavior of the system. Then, the

Table 1 Geometric parameters of 6804 ball bearing

Parameters	Symbols	Values	Units
The inner race's diameter	D_{i}	0.02	m
The inner raceway's diameter	d_{i}	0.02379	m
Outer raceway diameter	d_{o}	0.02802	m
Outer race diameter	D_{o}	0.032	m
Bearing width	W	0.007	m
Balls Diameter	d_{b}	0.003465	m
Radius of inner race groove	r_{i}	0,002138	m
Radius of the outer race groove	r_{o}	0,002183	m
Number of balls	N	11	
Elastic modulus of balls	E_1	200×10^9	GPa
Elastisite modulus of raceways	E_2	25×10^8	GPa
Poisson ratio of balls	ν_1	0.3	
Poisson ratio of raceways	ν_2	0.46	
Unbalance eccentricity	E_{s}	1×10^{-7}	m
Time step	Δt	1/30000	sec
Initial condition,$[x_0; \dot{x}_0; y_0; \dot{y}_0]$	$\overline{x}_0$	$\left[1 \times 10^{-9}; 0; 0; 0\right]$	m

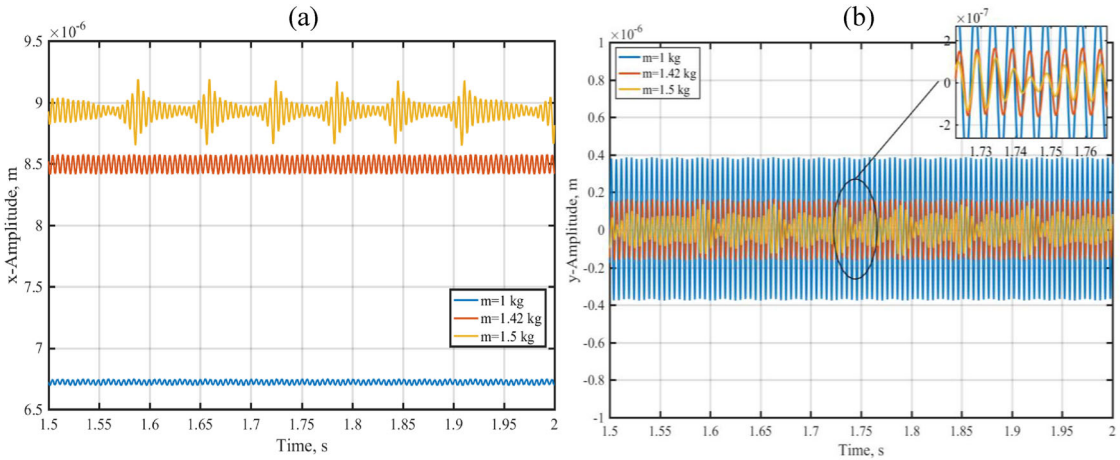

Fig. 3 The response of the system under different rotor mass for the rotational speed, $N = 2500$ rpm, **a** along x-direction, **b** along y-direction

response's nonlinear dynamic characteristics, such as periodicity, chaos, etc., were classified and identified with orbit plots, phase diagrams, Poincare maps, and spectrum graphs.

Figure 3 shows the steady-state responses of the system along x- and y-direction under rotational speed, $N = 2500$ rpm for different rotor masses. The rotor oscillates around the bearing center along the y-direction. However, the steady-state equilibrium positions of the rotor along the x-direction move away from the bearing center when the rotor increases in weight due to the gravitational effect, as expected. Moreover, the peak-to-peak amplitude along the x-direction increases when the rotor mass increases. On the other hand, the characteristics of the steady-state responses along both axes are also affected by the rotor mass, and the behavior of the responses varies from periodic to chaotic. In the contact model, the rotor mass determines the critical deformation, as well as the pressure force on the inner and outer raceway of the bearing. Thus, the characteristics of the contact can transform from elastic to elastoplastic; in other words, existing force is due to contact. As a result, it could be seen from Fig. 3 that the dynamic characteristics of the response strongly relate to the contact characteristics, as expected.

The rotational speed is another parameter that affects the bearing-rotor system's dynamic characteristics. Figure 4 shows the steady-state responses of the system under rotor mass of M = 1.5 kg, for different rotational speeds. It can be seen that the peak-to-peak amplitude of the responses is higher for low rotating speed, and the behavior of the responses is further impacted by rotational speed due to unbalance, as expected.

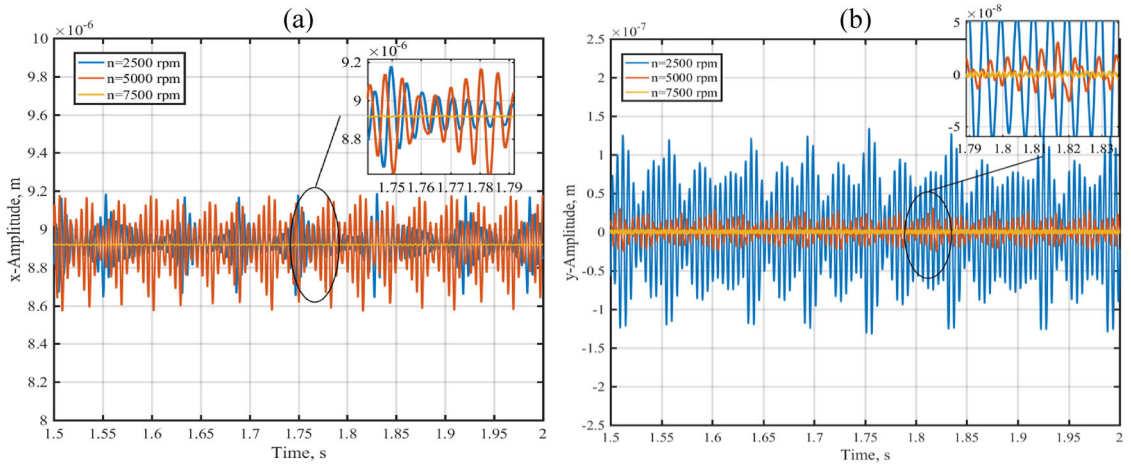

Fig. 4 The response of the system under different rotational speed for the rotor mass, $M = 1.5$ kg, **a** along x-direction, **b** along y-direction

3.1 Effects of the rotor mass on the system's nonlinear response

In order to detail the effect of rotor mass, the system is simulated for the rotor mass from 0.2 to 2.5 kg under a constant rotating speed of $N = 2500$ rpm. The spectra of the steady-state response are illustrated as waterfall diagrams given in Fig. 5. It could be seen that the dynamic behavior of the system is complex, and the peak values appear at the frequency of 198 Hz dominates in the waterfall diagrams, which corresponds to the computation of the ball passage frequency depending on the rotational speed. In addition, the superharmonic components of it are also seen at 396 Hz and 594 Hz in both diagrams. Besides, although the amplitude is very small, the synchronous vibrations (1X) at the frequency of 41.6 Hz are observed in the waterfall diagrams. On the other hand, it could be seen that when the rotor mass reaches 1.5 kg, the frequency components become sprawl, and lots of peak values exist in the waterfall diagrams. Although this characteristic is visible within mass from 1.5 to 2.25 kg, the disordered frequency components become to vanish when it exceeds 2.25 kg. After 2.25 kg, the ball passage frequency and its superharmonic components dominate the diagram again. When the rotor mass exceeds 1.4 kg, the elastic contact between the ball and inner/outer raceway begins to transform into the elastoplastic contact, and there exists a transition region. As mass increases, the contact is fully elastoplastic, and the dynamic attitude of the system is strongly affected by this transition. On the other hand, it could be seen that while the x-amplitude reaches the maximum values at 1.66 kg, the y-amplitude is the maximum at 1 kg. Therefore, it could be said that the resonance phenomenon occurs at 0.92 kg and 1.66 kg, and the critical speed of the system along the x- and y-direction are coincident with ball passage frequency.

The peak-to-peak amplitudes of the steady-state response are also calculated, and their variations with the rotor mass are shown in Fig. 6. The system's critical speeds are visible in plots. Besides, it could be said that the peak-to-peak responses indicate a complex dynamic behavior of the system in both directions when the rotor mass is within a specific region of around 1.5 kg. However, the amplitudes are smooth apart from this region.

An algorithm was developed to extract the bifurcation diagrams in this study. This algorithm determines peak points of the steady-state portion of the time series and stores them in a matrix sized by the length of the bifurcation parameter and the number of the extracting peaks. Then, the diagram is created by plotting with dots concerning matrix values and bifurcation parameters. Figure 7 shows the bifurcations and dynamic behavior of the steady-state responses under rotational speed, $N = 2500$ rpm, when the rotor mass increases from 0.2 to 2.5 kg. When the rotor mass is lower than M = 1.5 kg, the steady-state response of the rotor seems periodic in both x- and y-direction, and the resonance phenomenon occurs at M = 0.91 kg along y-direction (see Fig. 7b) for rotating speed, $N = 2500$ rpm. When it closes to M = 1.5 kg, the chaotic motion begins in both x- and y-direction, and the chaotic motion continues to appear up to M = 1.7 kg. When it is lower than 1.5 kg, there is elastic contact between the ball and inner/outer races.

However, elastoplastic contact starts to occur when it reaches and exceeds 1.5 kg. Therefore, the dynamic behavior of the response enters the chaotic motion, and even though the chaotic motion transforms to periodic motion when the rotor mass exceeds 1.7 kg, it stays in the quasiperiodic motion. On the other hand, the

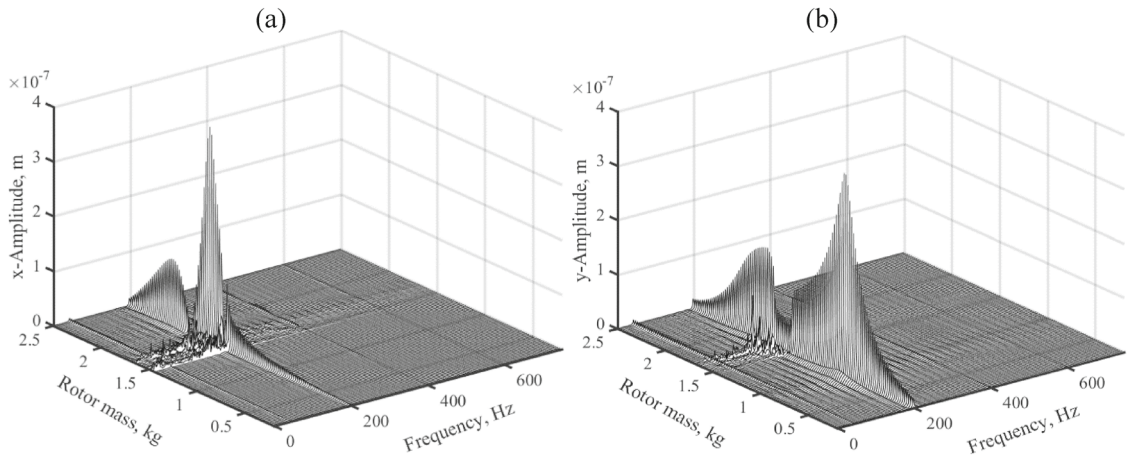

Fig. 5 Waterfall diagram of unbalanced response of the system for the rotational speed, $N = 2500$ rpm, **a** along x-direction, **b** along y-direction

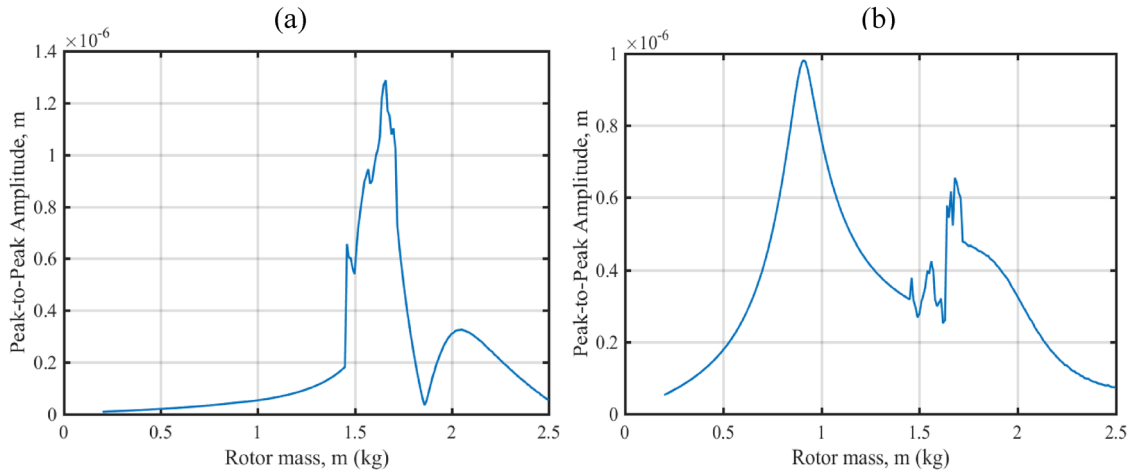

Fig. 6 Peak-to-peak response of the system for the rotor mass, $N = 2500$ rpm, **a** along x-direction, **b** along y-direction

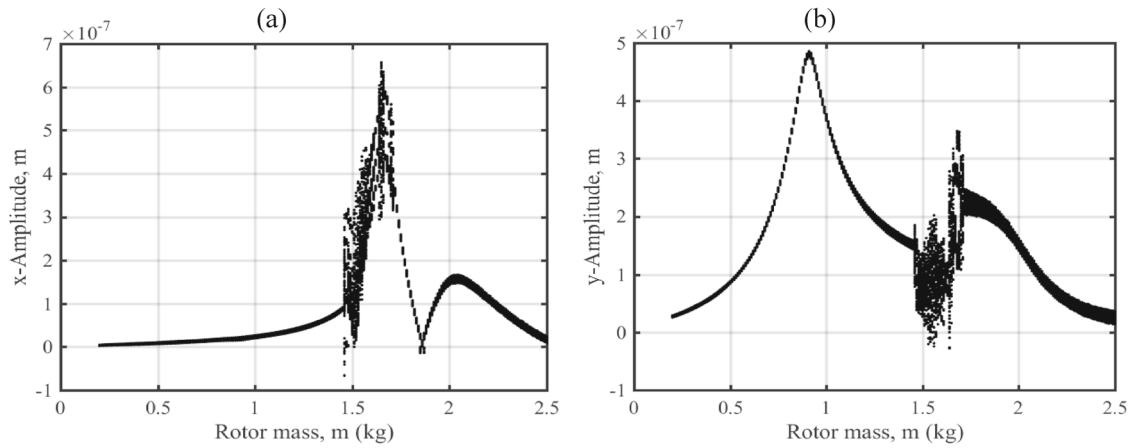

Fig. 7 Bifurcation diagram of unbalanced response of the system for the rotor mass, $N = 2500$ rpm **a** along x-direction, **b** along y-direction

resonance occurs at M = 1.66 kg in the x-direction (see Fig. 7a) when the system behaves in chaotic motion. Then, the dynamic behavior of the system in both directions, transitions from chaotic motion to quasiperiodic motion.

The Poincare maps were determined by considering successive intersections of a trajectory with a codimension-one surface. In order to conduct a detailed analysis of the behavior of the response, the orbit graphs, phase portraits, Poincare diagrams, and the spectrums of the responses are plotted for the critical regions determined by the bifurcation analysis, and they are shown in Figs. 8 and 9. When the rotor mass is lower than 1.46 kg, the behavior of the motion seems quasiperiodic according to Fig. 8a1–d1 given for M = 1 kg. When it is 1.46 kg, the Poincare map given in Fig. 8c2 shows broad and distributed points; in addition, the spectrum has a wide band at the bottom of the peak frequency (see Fig. 8d2). Moreover, it could be seen from Fig. 8a2 that the rotor center moves inside a complex whirl. When it is 1.47 kg by slightly increasing, although the dynamic behavior transforms to quasiperiodic motion according to orbit plot, Poincare maps, and the spectrum given in Fig. 8a3–d3, the response behavior enters chaotic, again at 1.48 kg (see Fig. 8a4–d4). After the dynamic behavior of the system stays in chaotic motion within a range of 1.48–1.62 kg, when the rotor mass is 1.63 kg, the Poincare map given in Fig. 8c5 shows the 3 distinct points; moreover, a total of three dominant peaks observe in the spectrum graphs illustrated in Fig. 8c5; therefore, the dynamic behavior is period-3. On the other hand, it could be seen from Fig. 9a1–d1 and a2–d2 that the motion transforms from chaotic to period-3 at 1.64 kg, then from chaotic to period-3 at 1.67 kg. When it is 1.69 kg, according to Poincare maps, as well as the spectrum graph given in Fig. 9c3 and d3, respectively, it could be said that the period-4 motion occurs in the response. When it exceeds 1.72 kg, the dynamic behavior enters the quasiperiodic motion and stays in this behavior (see Fig. 9a5–d5).

3.2 Effects of the shaft speed on the system's nonlinear response

To examine the impact of rotational speed, the ball bearing-rotor system simulated for the rotational speed within the range of 0–20,000 rpm and the rotor mass, M = 1.42 kg. And the spectra of the response are illustrated as waterfall diagrams given in Fig. 10. It could be seen that the dynamic behavior of the system is complex in low-speed regions, and the synchronous vibration (1X) dominates in the waterfall diagrams along the x-direction and y-direction. Besides, the superharmonics of the synchronous vibration are also visible in waterfall diagrams. In the waterfall diagram of the steady-state response along the x-direction, the synchronous vibration reaches a peak value at 200 Hz and the resonance phenomenon occurs.

On the other hand, it is seen from Fig. 10b that the resonance frequency is 170 Hz in the y-direction. Furthermore, the critical speeds of the system coincide with supersynchronous vibration, and peak values are visible in both waterfall diagrams at superharmonics of the synchronous vibrations. On the other hand, the waterfall diagrams show lots of sprawled peaks at different frequency components in the speed range between 2500 and 5000 rpm. And these peaks are more visible on the waterfall diagram of the response along the x-direction. Although these peaks cast doubt on the contact characteristic transformation from elastic to elastoplastic in this region, detection of the contact transformation is complicated on the waterfall diagrams. However, in the simulation, it was assumed that the rotor was mass unbalanced. Therefore, the unbalanced force acting on the response grows up, and so the characteristic of the contact can change as the rotor accelerates.

Figure 11a and b shows the peak-to-peak amplitudes of the steady-state response. According to variations, the critical speeds of the system are visible, and it along the x-direction is 12,000 rpm while it is 10,050 rpm in the y-direction. On the other hand, after the peak-to-peak responses reach critical speeds, it could be said that the responses indicate a complex dynamic behavior in both directions. When the rotational speed is within a range of 2500–5000 rpm, peaks around 2500 rpm and 5000 rpm are observed in the x-direction, whereas a peak around 2500 rpm is observed in the y direction.

Figure 12 shows the bifurcations and dynamic behavior of the x- and y-directional steady-state responses under rotor mass, M = 1.42 kg when the rotor accelerates up to 20,000 rpm. When the rotational speed is lower than 2500 rpm, the response along the x-direction seems periodic; however, bifurcations are visible in the response along the y-direction. After it exceeds 2500 rpm, the dynamic behaviors of the response along the y-direction also transform the periodic. Then, when it closes to 5000 rpm, it is seen from Fig. 12 that the chaotic motion is observed in both directions. However, when it slightly increases and it reaches 5000 rpm, a bifurcation in the responses of the system in both directions starts. After 5000 rpm, the dynamic behavior transforms from chaotic to quasiperiodic motion, and the quasiperiodic motion continues to stay in the responses until 7500 rpm. When it exceeds 7500 rpm, the response enters the period-1 motion, and

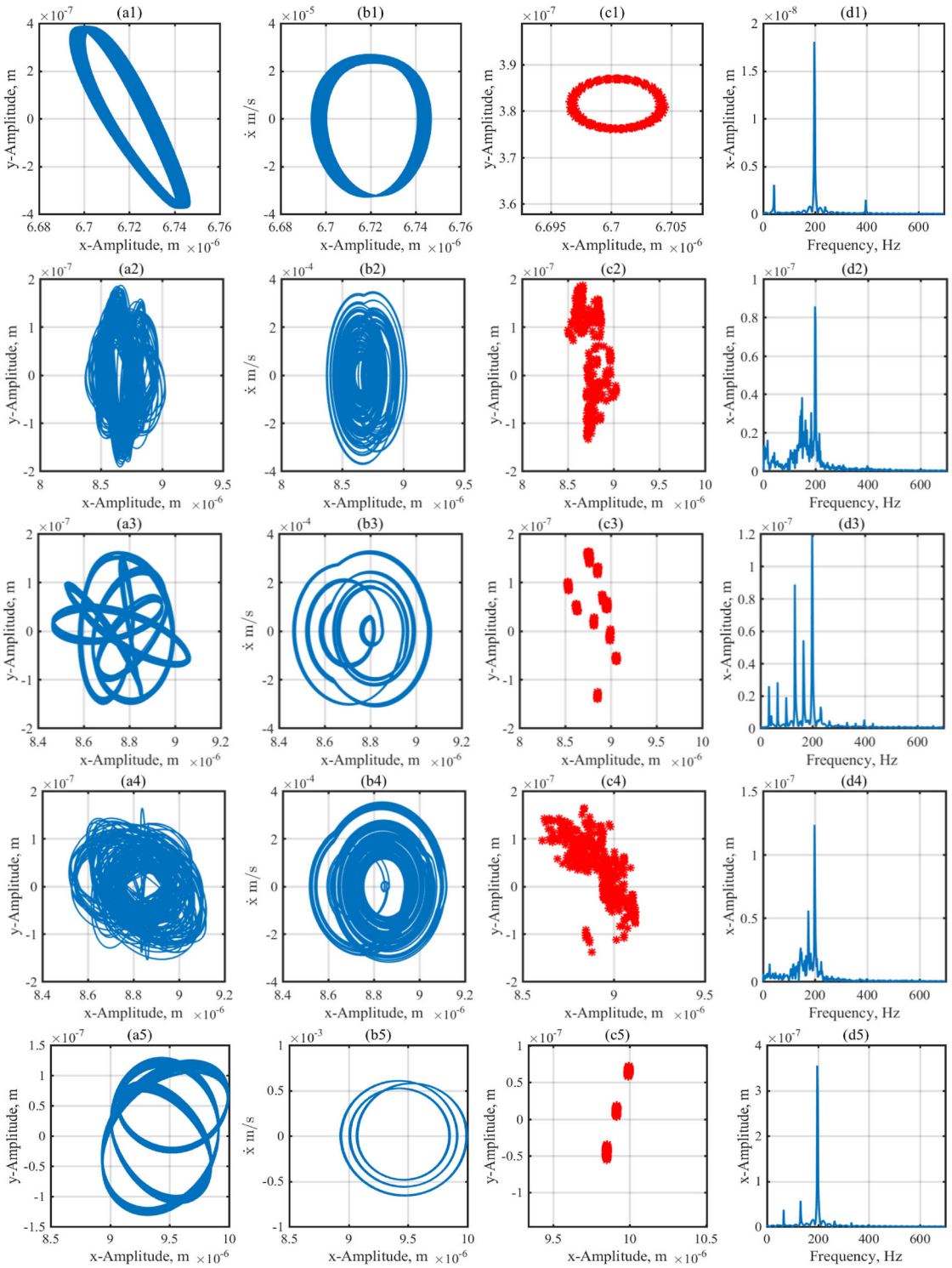

Fig. 8 Orbit plots, phase portraits, Poincare maps, and spectrums of the unbalanced response of the system, under the rotating speed, $N = 2500$ rpm **a1–d1**, M = 1 kg, **a2–d2** M = 1.46 kg, **a3–d3** M = 1.47 kg, **a4–d4** M = 1.48 kg, **a5–d5**) M = 1.63 kg

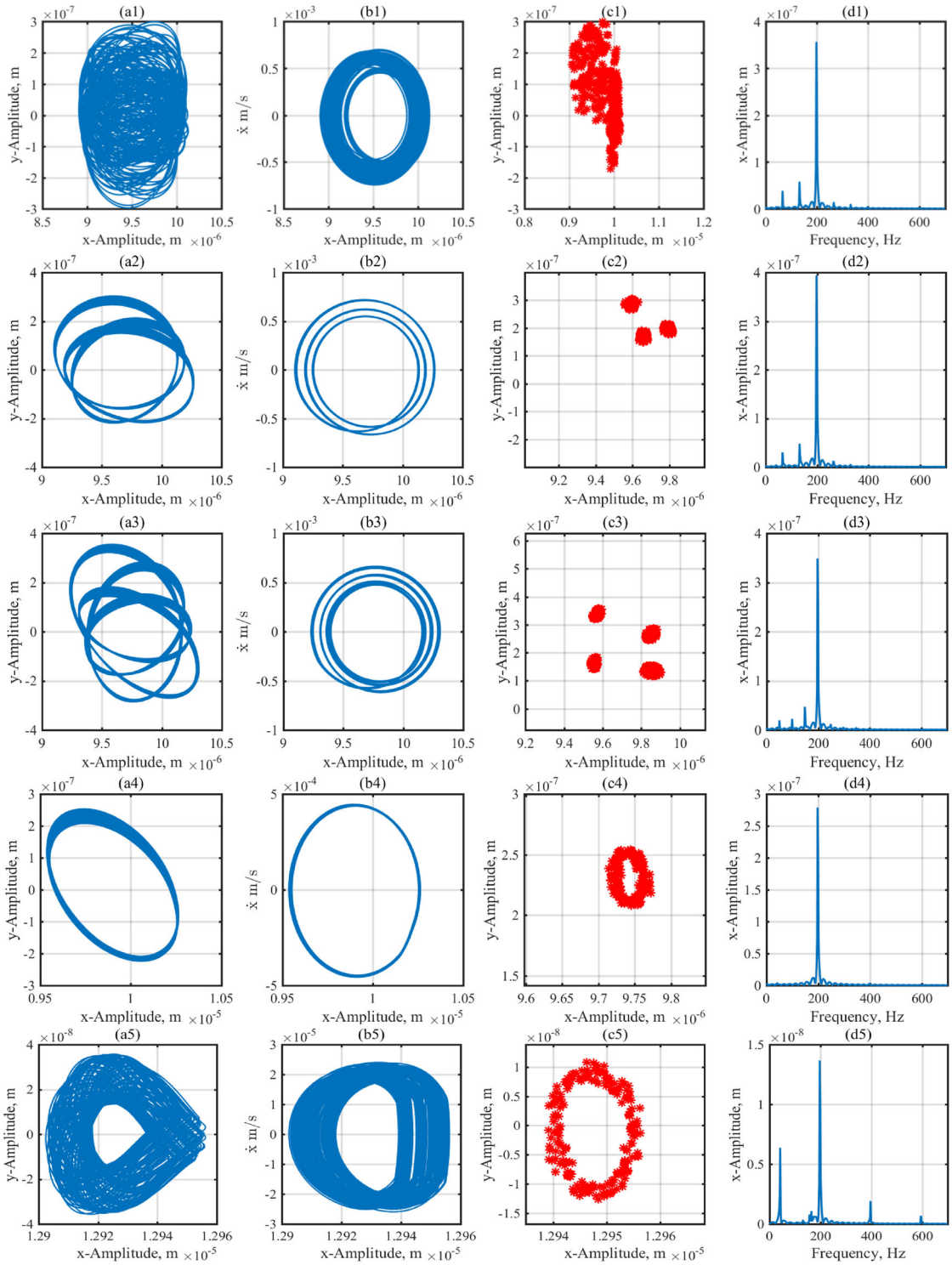

Fig. 9 Orbit plots, phase portraits, Poincare Maps, and spectrums of the unbalanced response of the system, under the rotating speed, $N = 2500$ rpm **a1–d1**, M = 1.64 kg, **a2–d2** M = 1.67 kg, **a3–d3** M = 1.69 kg, **a4–d4** M = 1.72 kg, **a5–d5** M = 2.5 kg

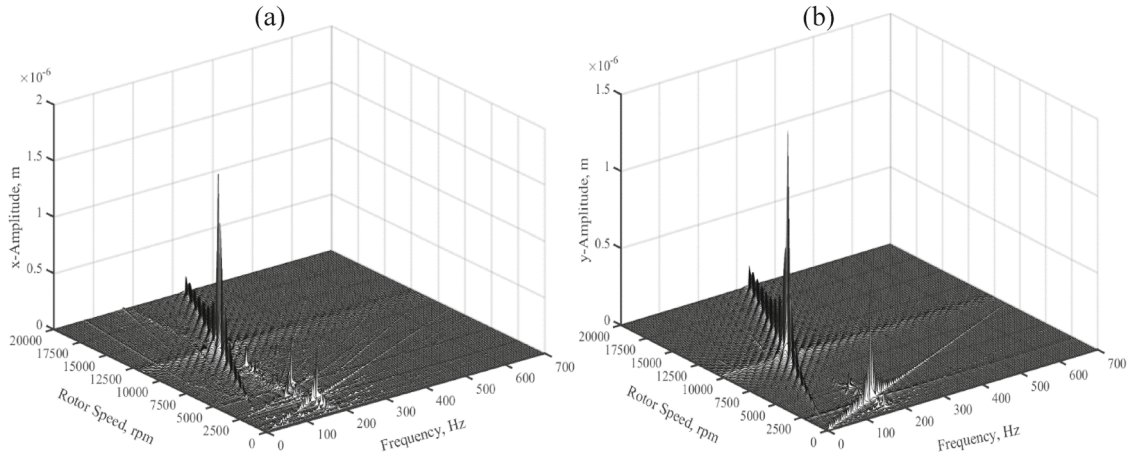

Fig. 10 Waterfall diagram of unbalanced response of the system for the rotational speed, $M = 1.42$ kg, **a** along x-direction, **b** along y-direction

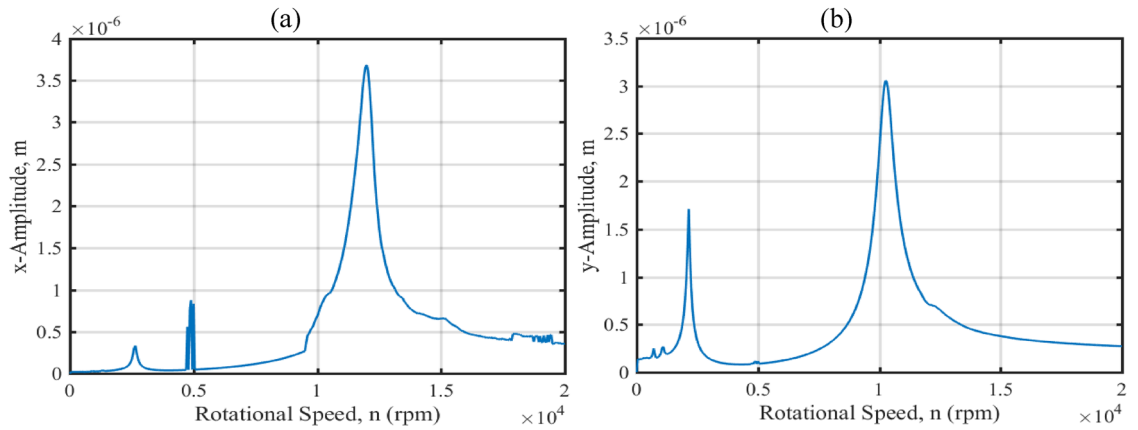

Fig. 11 Peak-to-peak response of the system for the rotor mass, $M = 1.42$ kg, **a** along x-direction, **b** along y-direction

it stays until 9500 rpm. When the rotor speed reaches 9550 rpm, the chaotic motion exists in the response, and the chaos in the response continues until 9800 rpm. After chaotic motion, the dynamic behavior of the system enters random quasiperiodic motion, and it continues until 10,500 rpm, and then the response behaves in period-1 motion. At 12,500 rpm, the period-1 motion transforms the quasiperiodic motion. It is seen from Fig. 12a that when the rotor speed exceeds 12,500 rpm, although the line becomes thick by getting thinner and vice versa, the dynamic behavior of the system stays in quasiperiodic motion.

In order to detailed analysis of the behavior of the response, the orbit graphs, phase portraits, Poincare diagrams, and the spectrums of the responses are plotted for the critical regions determined by the bifurcation analysis, and they are shown in Figs. 13, 14 and 15. There are a total of four distinct points in the Poincare map at 700 rpm according to Fig. 13c1, whereas there are a total of three points at 1250 rpm as seen in Fig. 13c2. Besides, it is seen in spectrum graphs that the number of the peak components is the same as the point number in the Poincare maps. Therefore, the behavior of the motion seems the period-T when the rotational speed is lower than 2500 rpm. Moreover, when the rotational speed increases, the period-4 motion transforms the period-3 motion. Conversely, in cases when it reaches 2500 rpm, the dynamic behavior enters period-2 motion according to orbit plots and Poincare maps given in Fig. 13a3 and c3. However, when it exceeds 2500 rpm and reaches 3750 rpm, points in the Poincare map form a closed curve according to Fig. 13c4 even though the rotor center is in a complex whirl as seen in orbit plot (see Fig. 13a4). Therefore, the response starts to behave a quasiperiodic characteristic, and the dynamic behavior stays in quasiperiodic motion until 4900 rpm (see Fig. 13a4–d4). After 4900 rpm, it is seen from Fig. 13c5 that the closed curve shears off, and points form a shape as two distinct arcs and the quasiperiodic motion transforms the quasiperiodic-2 motion. At 5000 rpm, the response enters chaotic motion. In Fig. 14a1–d1, broad and distributed points, a wide band at the bottom

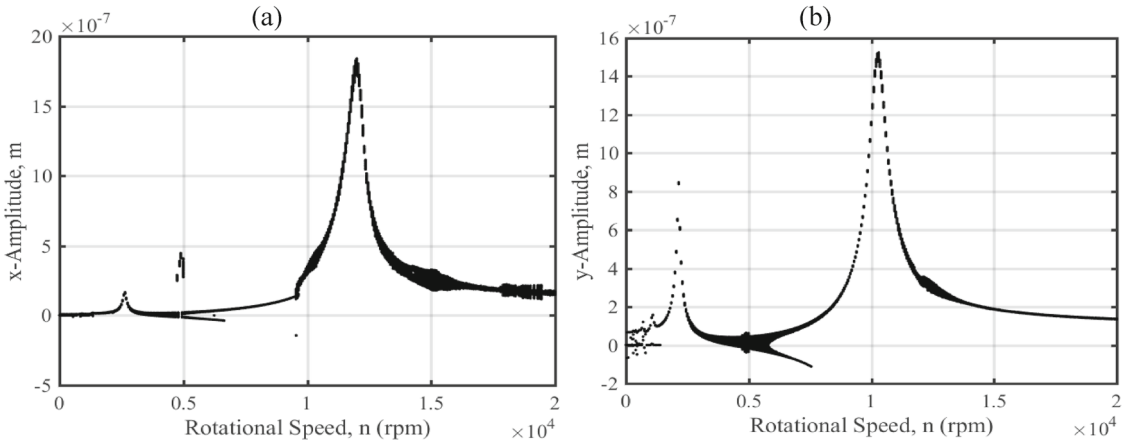

Fig. 12 Bifurcation diagram of unbalanced response of the system for the rotor mass, $M = 1.42$ kg, **a** along x-direction, **b** along y-direction

of peak frequency in the spectrum plot, moreover, complex whirl in orbits plots are evidence of the chaotic motion at 5000 rpm. However, the chaotic motion takes a short time, and transforms the quasiperiodic-2 motion according to Fig. 14a2–d2. The quasiperiodic-2 motion continues in a range of 5050–7450 rpm, and when it 7500 rpm, the quasiperiodic motion transforms period-1 motion as seen in Fig. 14a3–d3. However, as it is 9600 rpm, the dynamic behavior enters the chaotic motion according to Fig. 14a4–d4. Then, the chaotic behavior transforms again the period-1 motion at 10,500 rpm.

On the other hand, when the rotational speed exceeds 10,500 rpm, as seen in Fig. 15a1–d1, the period-1 motion transforms the random quasiperiodic motion until 15,000 rpm. Two nested circles are observed in Fig. 15c2; therefore, the behavior could be described as to be the quasiperiodic-2 motion at 15,000 rpm (see Fig. 15a2–d2). The quasiperiodic-2 motion is observed in the response until 16,000 rpm. However, when the rotational speed exceeds 16,000 rpm, it turns the quasiperiodic-1 motion, as seen in Fig. 15a3–d3, and continues until the end of the speed range.

During simulation, the numerical solution algorithm defines a specific number to identify the contact characteristics at each ball, and it stores these numbers in a matrix. To present the results, firstly the number of ball which is under the elastic or elastoplastic contact characteristics is found by extracting the steady-state portion of the time series from storing matrix, and then the total number of the balls is illustrated on a graph considering the contact characteristics. To investigate the connection between the dynamic behavior of the system and plasticity, the contact type between balls and the inner/outer raceway was determined from Eq. 1 and recorded at each time step in the simulation. Figure 16a shows the maximum number of balls at the elastoplastic contact under increasing rotor mass at 2500 rpm. All balls are in elastic contact with raceways in a range of rotor mass, 0.2–1.45 kg. However, when it reaches 1.46 kg, the elastoplastic contact starts, and two balls are elastoplastic contact. When this result is evaluated with the results from the bifurcation and nonlinear dynamic analysis (see Figs. 5, 6 and 7), it could be said that the system's dynamic response begins to exhibit chaotic behavior at the elastoplastic contact.

Furthermore, when the number of balls in elastoplastic contact increases from 2 to 3, it could be emphasized that the dynamic behavior varied from chaotic to quasiperiodic and vice versa. On the other hand, Fig. 16b shows the maximum number of balls at the elastoplastic contact under increasing rotational speed when the rotor-bearing system operates under M = 1.42 kg. It could be seen from Fig. 16b that there are no balls in elastoplastic contact until 4950 rpm, and the chaotic behavior starts in the response of the system (see Fig. 16b). However, when it is 4950 rpm, there is one ball in elastoplastic contact, and after an increment of the speed, the contact characteristic transforms again elastic contact. Nevertheless, when it exceeds 9600 rpm, elastoplastic contact between balls and raceways occurs, and after 9600 rpm, there is at least one ball in elastoplastic contact. When the rotational speed increases, the dynamic response can coincide with synchronous vibration, as well as its harmonic, so the response can magnify. Therefore, the characteristic of the contact varies depending on the rotational speed. However, it could be said that the behavior of the system is strongly affected by the number of balls in elastoplastic contact, as expected.

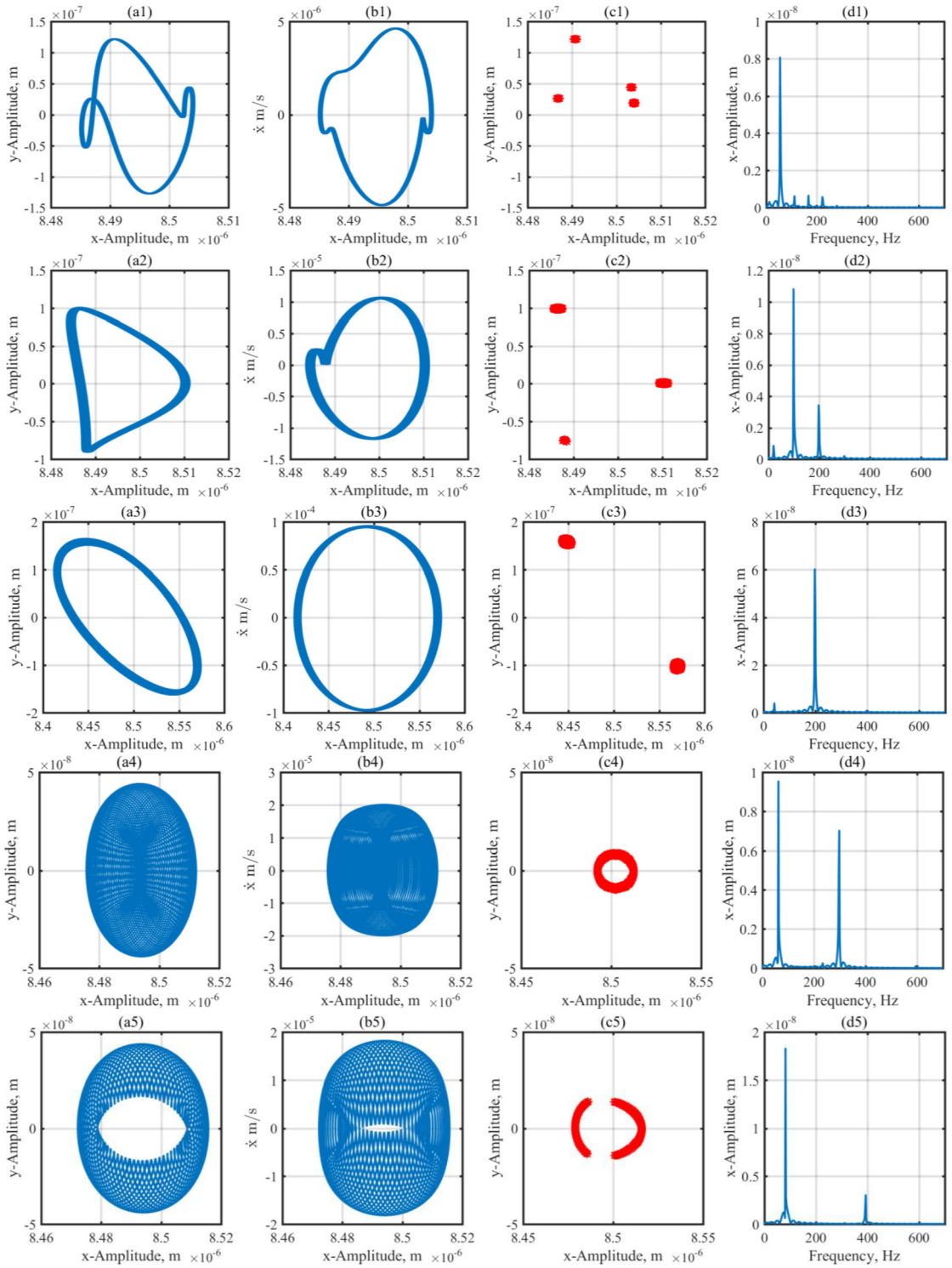

Fig. 13 Orbit plots, phase portraits, Poincare Maps, and spectrums of the unbalanced response of the system, under the rotating speed, $M = 1.42$ kg **a1–d1**, $N = 700$ rpm, **a2–d2** $N = 1250$ rpm, **a3–d3** $N = 2500$ rpm, **a4–d4** $N = 3750$ rpm, **a5–d5** $N = 4950$ rpm

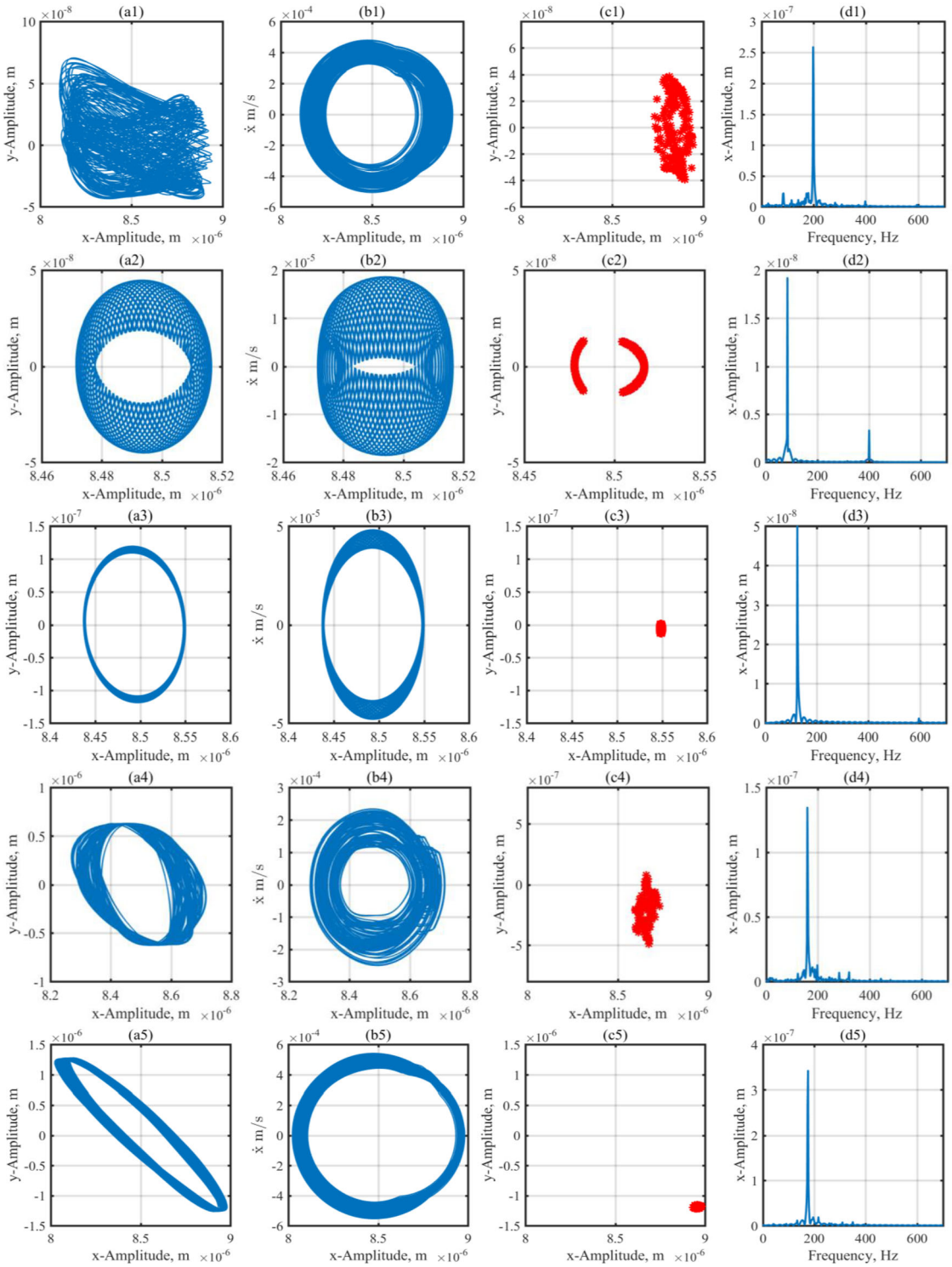

Fig. 14 Orbit plots, phase portraits, Poincare Maps, and spectrums of the unbalanced response of the system, under the rotating speed, $M = 1.42$ kg **a1–d1**, $N = 5000$ rpm, **a2–d2** $N = 5050$ rpm, **a3–d3** $N = 7500$ rpm, **a4–d4** $N = 9600$ rpm, **a5–d5** $N = 10{,}500$ rpm

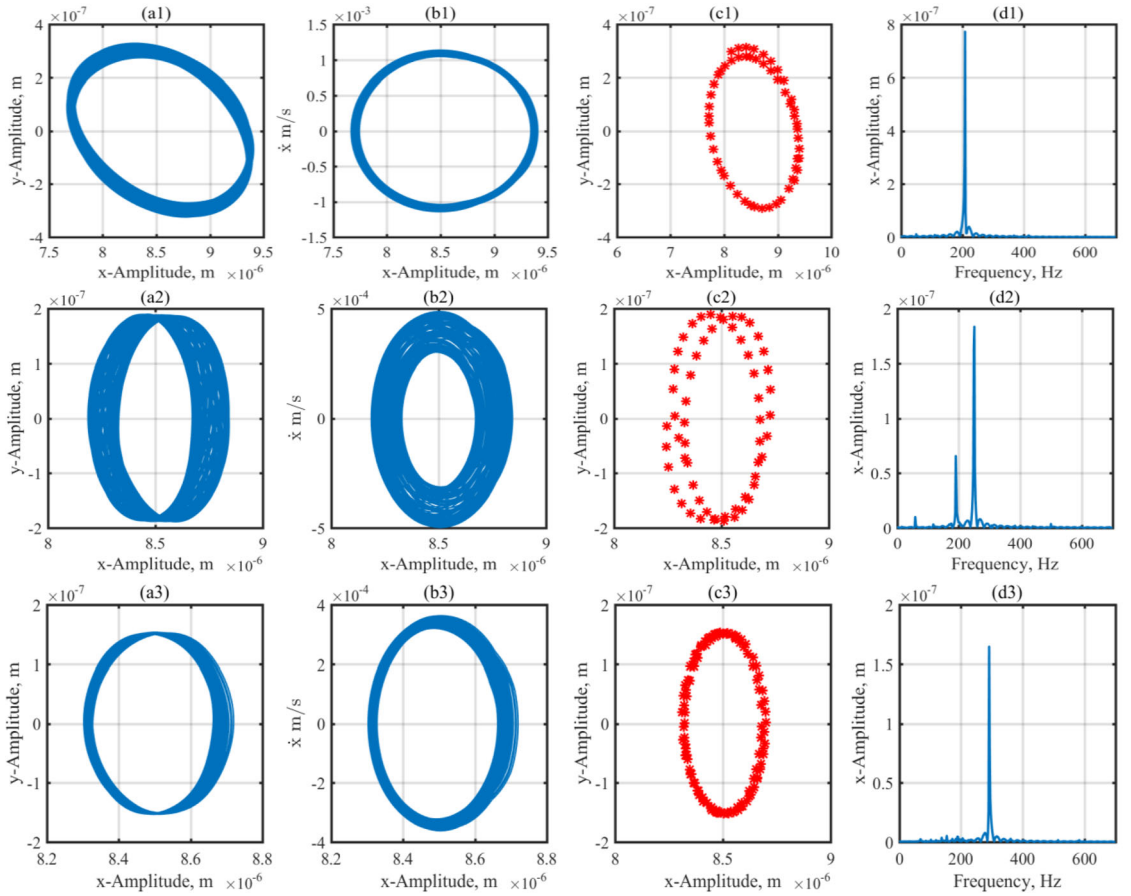

Fig. 15 Orbit plots, phase portraits, Poincare Maps, and spectrums of the unbalanced response of the system, under the rotating speed, $M = 1.42$ kg **a1–d1**, $N = 12{,}500$ rpm, **a2–d2** $N = 15{,}000$ rpm, **a3–d3** $N = 17{,}500$ rpm

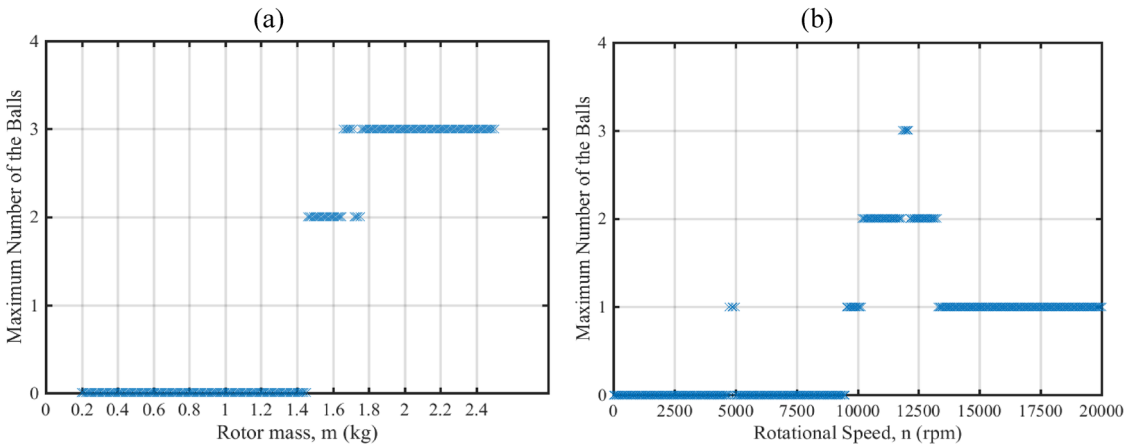

Fig. 16 The number of balls in elastoplastic contact, **a** Variation with rotor mass ($N = 2500$ rpm), **b** variation with rotational speed ($M = 1.42$ kg)

4 Conclusion

The nonlinear dynamic behavior and bifurcation characteristic of the rotor supported by hybrid polymer ball bearing have been analyzed. The modeling of the contact between the balls and the polymer raceways takes into account the viscoelastic properties of the structure. Three primary phases of the contact—elastoplastic, completely plastic, and elastic—have been identified, and corresponding contact forces have been developed for each. The shaft speed and its weight have been chosen as bifurcation parameters, and the steady-state response of the system has been investigated with time and frequency domains analysis methods. The simulation results show that the contact characteristics affect the dynamic behavior of the system. The *T*-periodic, quasiperiodic, quasiperiodic-*n,* and chaotic motions could exist in the response. When the contact is in the elastic phase, the response changes from periodic to quasiperiodic motion. However, when the contact in any ball enters the elastoplastic phase, the dynamic behavior is to be chaotic. It is also affected by the shaft speed, because the contact characteristics changes with the unbalance force with the increase in the rotational speed.

The study can be expanded by using the finite element method and experimental studies. For defect detection, studies can be carried out using machine learning methods to investigate whether the bearings have moved into the elastoplastic region.

Acknowledgements The study that was presented was financed by the Gazi University Scientific Research Projects Unit under Grant No. 06/2018-08.

Author contributions B.K.D. and A. D. wrote the main manuscript text and T.K. reviewed the manuscript made the necessary corrections.

Funding Open access funding provided by the Scientific and Technological Research Council of Türkiye (TÜBİTAK).

Data availability No datasets were generated or analyzed during the current study.

Declarations

Conflict of interest The authors declare no competing interests.

References

1. Ghaednia, H., Wang, X., Saha, S., Xu, Y., Sharma, A., Jackson, R.L.: A review of elastic–plastic contact mechanics. Appl. Mech. Rev. **69**(6), 060804 (2017)
2. Kogut, L., Etsion, I.: Elastic-plastic contact analysis of a sphere and a rigid flat. J. Appl. Mech. **69**(5), 657–662 (2002)
3. Lin, L.P., Lin, J.F.: A new method for elastic-plastic contact analysis of a deformable sphere and a rigid flat. J. Tribol. **128**(2), 221–229 (2006)
4. Zhang, W., Chen, J., Wang, C., Liu, D., Zhu, L.: Research on elastic–plastic contact behavior of hemisphere flattened by a rigid flat. Materials **15**(13), 4527 (2022)
5. Wang, Z.Q.: A compact and easily accepted continuous model for the elastic-plastic contact of a sphere and a flat. J. Appl. Mech. **80**(1), 014506 (2013)
6. Wang, F.S., Block, J.M., Chen, W.W., Martini, A., Zhou, K., Keer, L.M., Wang, Q.J.: A multilevel model for elastic-plastic contact between a sphere and a flat rough surface. **131**(2), 021409 (2009)
7. Malayalamurthi, R., Marappan, R.: Elastic-plastic contact behavior of a sphere loaded against a rigid flat. Mech. Adv. Mater. Struct. **15**(5), 364–370 (2008)
8. Jamari, J., Schipper, D.J.: Experimental investigation of fully plastic contact of a sphere against a hard flat. J. Tribol. **128**(2), 230–235 (2006)
9. Ghaednia, H., Pope, S.A., Jackson, R.L., Marghitu, D.B.: A comprehensive study of the elasto-plastic contact of a sphere and a flat. Tribol. Int. **93**, 78–90 (2016)

10. Etsion, I., Levinson, O., Halperin, G., Varenberg, M.: Experimental investigation of the elastic–plastic contact area and static friction of a sphere on flat. J. Trib. **127**(1), 47–50 (2005)
11. Sahoo, P., Chatterjee, B., Adhikary, D.: Finite element based elastic-plastic contact behavior of a sphere against a rigid flat-effect of strain hardening. Int. J. Eng. Technol. **2**(1), 1–6 (2010)
12. Hardy, C., Baronet, C., Tordion, G.: The elasto-plastic indentation of a half-space by a rigid sphere. Int. J. Numer. Methods Eng. **3**(4), 451–462 (1971)
13. Sinclair, G., Follansbee, P., Johnson, K.: Quasi-static normal indentation of an elasto-plastic half-space by a rigid sphere—II. Results. Int. J. Solids Struct. **21**(8), 865–888 (1985)
14. Follansbee, P., Sinclair, G.: Quasi-static normal indentation of an elasto-plastic half-space by a rigid sphere—I: analysis. Int. J. Solids Struct. **20**(1), 81–91 (1984)
15. Tabor, D.: The Hardness of Metals. Oxford University Press, New York (2000)
16. Ishlinskii, A.: The problem of plasticity with axial symmetry and Brinell's test. J. Appl. Math. Mech. **8**, 201–224 (1944)
17. Richmond, O., Morrison, H., Devenpeck, M.: Sphere indentation with application to the brinell hardness test. Int. J. Mech. Sci. **16**(1), 75–82 (1974)
18. Ye, N., Komvopoulos, K.: Indentation analysis of elastic-plastic homogeneous and layered media: criteria for determining the real material hardness. ASME J. Tribol. **125**(4), 685–691 (2003)
19. Komvopoulos, K., Ye, N.: Three-dimensional contact analysis of elastic-plastic layered media with fractal surface topographies. ASME J. Tribol. **123**(3), 632–640 (2001)
20. Kogut, L., Komvopoulos, K.: Analysis of the spherical indentation cycle for elastic-perfectly plastic solids. J. Mater. Res. **19**(12), 3641–3653 (2004)
21. Bartier, O., Hernot, X., Mauvoisin, G.: Theoretical and experimental analysis of contact radius for spherical indentation. Mech. Mater. **42**(6), 640–656 (2010)
22. Brake, M.: An analytical elastic-perfectly plastic contact model. Int. J. Solids Struct. **49**(22), 3129–3141 (2012)
23. Brizmer, V., Zait, Y., Kligerman, Y., Etsion, I.: The effect of contact conditions and material properties on elastic-plastic spherical contact. J. Mech. Mater. Struct. **1**(5), 865–879 (2006)
24. Kharaz, A., Gorham, D., Salman, A.: Accurate measurement of particle impact parameters. Meas. Sci. Technol. **10**(1), 31 (1999)
25. Brake, M.: An analytical elastic plastic contact model with strain hardening and frictional effects for normal and oblique impacts. Int. J. Solids Struct. **62**, 104–123 (2015)
26. Yau, L.C., Zamri, W.F.H.W., Din, M.F.M., Fadhlina, I., Mohamed, A.A.: Elastic and Elasto-plastic contact behavior on ball bearing. Int. J. Innov. Technol. Exp. Eng. **8**(6), 438 (2020)
27. Tiwari, M., Gupta, K., Prakash, O.: Dynamic response of an unbalanced rotor supported on ball bearings. J. Sound Vib. **238**(5), 757–779 (2000)
28. Gupta, T. C., Gupta, K., Sehgal, D. K.: Instability and chaos of a flexible rotor ball bearing system: an investigation on the influence of rotating imbalance and bearing clearance. In: Turbo Expo: Power for Land, Sea, and Air (Vol. 133, No. 8), pp. 283-292 (2010)
29. Fukata, S., Gad, E.H., Kondou, T., Ayabe, T., Tamura, H.: On the radial vibration of ball bearing: computer simulation. Trans. Jpn. Soc. Mech. Eng. Ser. C **50**(457), 1703–1708 (1984)
30. Tiwari, M., Gupta, K., Prakash, O.: Effect of radial internal clearance of a ball bearing on the dynamics of a balanced horizontal rotor. J. Sound Vib. **238**(5), 723–756 (2000)
31. Wang, F., Jing, M., Yi, J., Dong, G., Liu, H., Ji, B.: Dynamic modelling for vibration analysis of a cylindrical roller bearing due to localized defects on raceways. Proc. Inst. Mech. Eng. Part K J. Multi-Body Dyn. **229**(1), 39–64 (2015)
32. Hess, D.P., Soom, A.: Normal vibrations and friction under harmonic loads: part I—Hertzian contacts. J. Tribol.-Trans. ASME **131**(1), 80–86 (1991)
33. Hess, D.P., Soom, A.: Normal vibrations and friction under harmonic loads: Part II—rough planar contacts. J. Tribol.-Trans. ASME **131**(1), 87–92 (1991)
34. Rigaud, E., Perret-Liaudet, J.: Experiments and numerical results on non-linear vibrations of an impacting Hertzian contact. Part 1: harmonic excitation. J. Sound Vib. **265**(2), 289–307 (2003)
35. Bichri, A., Belhaq, M., Perret-Liaudet, J.: Control of vibroimpact dynamics of a single-sided Hertzian contact forced oscillator. Nonlinear Dyn. **63**(1–2), 51–60 (2011)
36. Hou, L., Chen, Y., Fu, Y., Chen, H., Lu, Z., Liu, Z.: Application of the HB–AFT method to the primary resonance analysis of a dual-rotor system. Nonlinear Dyn. **88**(4), 2531–2551 (2017)
37. Zhang, Z., Rui, X., Yang, R., Chen, Y.: Control of period-doubling and chaos in varying compliance resonances for a ball bearing. J. Appl. Mech. **87**(2), 021005 (2020)
38. Jin, Y., Liu, Z., Yang, Y., Li, F., Chen, Y.: Nonlinear vibrations of a dual-rotor-bearing-coupling misalignment system with blade-casing rubbing. J. Sound Vib. **497**(6), 115948 (2021)
39. Lu, Z., Wang, X., Hou, L., Chen, Y., Liu, X.: Nonlinear response analysis for an aero engine dual-rotor system coupled by the inter-shaft bearing. Arch. Appl. Mech. **89**(7), 1275–1288 (2019)
40. Zhang, Z., Chen, Y., Cao, Q.: Bifurcations and hysteresis of varying compliance vibrations in the primary parametric resonance for a ball bearing. J. Sound Vib. **350**, 171–184 (2015)
41. Lu, Z., Liu, L., Wang, X., Ma, Y., Chen, H.: Dynamic modeling and bifurcation analysis of blade-disk rotor system supported by rolling bearing. Appl. Math. Model. **106**, 524–548 (2022)
42. Lu, H., Li, W., Shen, J., Chen, T., Sheng, L.: Dynamic characteristics analysis of rotor-bearing system considering bearing clearance and hybrid eccentricity. J. Vib. Eng. Technol. **12**(2), 2249–2263 (2024)
43. Li, F., Li, X., Li, B., Ma, H., Wen, B.: Nonlinear dynamic modeling and vibration analysis of bearing system considering shaft current damage. Mech. Based Des. Struct. Mach. **52**(2), 1190–1210 (2024)
44. Ambrożkiewicz, B., Litak, G., Georgiadis, A., Meier, N., Gassner, A.: Analysis of dynamic response of a two degrees of freedom (2-DOF) ball bearing nonlinear model. Appl. Sci. **11**(2), 787 (2021)

45. Chang, Z., Hou, L., Lin, R., Jin, Y., Chen, Y.: A modified IHB method for nonlinear dynamic and thermal coupling analysis of rotor-bearing systems. Mech. Syst. Signal Process. **200**, 110586 (2023)